



**HAL**  
open science

## **Actin network architecture can ensure robust centering or sensitive decentering of the centrosome**

Shohei Yamamoto, Jérémie Gaillard, Benoit Vianay, Christophe Guerin,  
Magali Orhant-Prioux, Laurent Blanchoin, Manuel Théry

### ► To cite this version:

Shohei Yamamoto, Jérémie Gaillard, Benoit Vianay, Christophe Guerin, Magali Orhant-Prioux, et al.. Actin network architecture can ensure robust centering or sensitive decentering of the centrosome. EMBO Journal, 2022, 41 (20), pp.e111631. 10.15252/emj.2022111631 . hal-03747547

**HAL Id: hal-03747547**

**<https://hal.science/hal-03747547>**

Submitted on 22 Aug 2022

**HAL** is a multi-disciplinary open access archive for the deposit and dissemination of scientific research documents, whether they are published or not. The documents may come from teaching and research institutions in France or abroad, or from public or private research centers.

L'archive ouverte pluridisciplinaire **HAL**, est destinée au dépôt et à la diffusion de documents scientifiques de niveau recherche, publiés ou non, émanant des établissements d'enseignement et de recherche français ou étrangers, des laboratoires publics ou privés.

1  
2 **Actin network architecture can ensure robust centering or sensitive**  
3 **decentering of the centrosome**  
4

5 Shohei Yamamoto<sup>1</sup>, Jérémie Gaillard<sup>1</sup>, Benoit Vianay<sup>2</sup>, Christophe Guerin<sup>1</sup>, Magali  
6 Orhant-Prioux<sup>1</sup>, Laurent Blanchoin<sup>1,2,\*</sup>, Manuel Théry<sup>1,2,\*</sup>  
7

8 1. University of Grenoble-Alpes, CEA, CNRS, INRA, Interdisciplinary Research Institute of Grenoble,  
9 UMR5168-LPCV, CytoMorpho Lab, Avenue des Martyrs, 38054 Grenoble, France

10 2. University of Paris, CEA, INSERM, Institut de Recherche Saint Louis, UMRS1160-  
11 HIPI, CytoMorpho Lab, Avenue Claude Vellefaux, 75010 Paris, France

12 \*Correspondence: [laurent.blanchoin@cea.fr](mailto:laurent.blanchoin@cea.fr) (L.B.), [manuel.thery@cea.fr](mailto:manuel.thery@cea.fr) (M.T.)  
13  
14

15 **Abstract**

16 The orientation of cell polarity depends on the position of the  
17 centrosome, the main microtubule-organizing center (MTOC). Microtubules (MTs)  
18 transmit pushing forces to the MTOC as they grow against the cell periphery. How the  
19 actin network regulates these forces remains unclear. Here, in a cell-free assay, we used  
20 purified proteins to reconstitute the interaction of a MT aster with actin networks of  
21 various architectures in cell-sized microwells. In the absence of actin filaments, the  
22 MTOC positioning was highly sensitive to variations in MT length. The presence of a  
23 bulk actin network limited MTs displacement, and MTOCs were held in place.  
24 In contrast, the assembly of a branched actin network along the well edges centered the  
25 MTOCs by maintaining an isotropic balance of pushing forces. An anisotropic peripheral  
26 actin network caused the MTOC to decenter by focusing the pushing forces. Overall, our  
27 results show that actin networks can limit the sensitivity of MTOC positioning to MT  
28 length and enforce robust MTOC centering or decentering depending on the isotropy of  
29 its architecture.  
30

31 **KEYWORDS**

32 Centrosome positioning / Microtubule / Actin network / MTOC / Synthetic cell

1 **Introduction**

2

3           The network of microtubules (MTs) supports the construction of cell body plan  
4 and directs its symmetry axes (Bornens, 2008; Meiring *et al*, 2020; Vignaud *et al*, 2012).  
5 The asymmetric organization of MTs directs the preferential orientation of vesicle  
6 transport and the position of key sensory organelles and thereby orients the main functions  
7 of polarized cells (Bornens, 2018; Harris *et al*, 2009; Vladar *et al*, 2012; Meiring *et al*,  
8 2020). The centrosome is the main microtubule-organizing center (MTOC), so its position  
9 is a key determinant of cell polarity (Tang & Marshall, 2012; Bornens, 2008). The  
10 positioning of centrosome, either at the cell center or at the cell periphery, in contact with  
11 the plasma membrane, is important for ciliogenesis, immune reactions, cell division,  
12 epithelial-to-mesenchymal transition or neuronal development (Pitaval *et al*, 2017b;  
13 Burute *et al*, 2017; Shao *et al*, 2020; Stinchcombe & Griffiths, 2014a; Elric & Etienne-  
14 Manneville, 2014).

15

16           Centrosome position is mainly controlled by combinations of pushing and  
17 pulling forces produced in the MT network (Letort *et al*, 2016; Burakov *et al*, 2003; Zhu  
18 *et al*, 2010; Pavin *et al*, 2012; Ma *et al*, 2014; Jimenez *et al*, 2021a). Homogeneous  
19 distribution of minus-end directed molecular motors, pulling on MTs in the cytoplasm or  
20 at the cell cortex, can enforce centrosome centering (Kimura & Kimura, 2011; Laan *et al*,  
21 2012; Koonce *et al*, 1999; Wu *et al*, 2011). Heterogeneous distribution of motors, due to  
22 local accumulations, can locally increase pulling forces and enforce MTOC decentering  
23 up to the contact with the plasma membrane (Dujardin *et al*, 2003; Yi *et al*, 2013).  
24 Regulation of centrosome positioning by such pulling forces is robust: centering, in the  
25 case of homogeneous distribution of motors, or peripheral positioning, in the case of  
26 heterogeneous distribution, are both poorly sensitive to variations of MT length (Letort  
27 *et al*, 2016). On the opposite, production of pushing forces is much more sensitive to  
28 variations of MT length and hence appears as a less reliable positioning mechanism. MT-  
29 based pushing is ineffective if MTs are too short to reach the spatial boundaries. Longer  
30 MTs may allow centering if their length corresponds precisely to the length of its  
31 confining region. However, MTs longer than this critical length will induce an abrupt

1 transition from centering to decentering (Pinot *et al*, 2009; Holy *et al*, 1997; Faivre-  
2 Moskalenko & Dogterom, 2002; Laan *et al*, 2012).

3

4           Actin networks are involved in centrosome positioning and have been proposed  
5 to modulate the pushing forces produced by MTs but the underlying mechanisms are  
6 obscure (Brito *et al*, 2005; Hale *et al*, 2011; Chevrier *et al*, 2002; Pelletier *et al*, 2020;  
7 Jimenez *et al*, 2021a; Burakov *et al*, 2003). There are numerous examples of physical  
8 interactions between MTs and actin filaments (Colin *et al*, 2018; Inoue *et al*, 2019;  
9 Farhadi *et al*, 2018; López *et al*, 2014; Jiang *et al*, 2012; Dogterom & Koenderink, 2019).  
10 Acting as obstacles, capturing sites or stabilizing sheaths, actin architectures may regulate  
11 and organize the spatial distribution of forces in the MT network, by either amplifying or  
12 buffering local asymmetries. However, how specific actin architectures, such as dense  
13 cortical networks, bundles of linear filaments or cytoplasmic mesh, specifically impact  
14 forces production and propagation along MTs, remains poorly understood.

15

16           Here, we show that the presence and architecture of actin networks affect the  
17 spatial distribution of MTs and the displacements of MTOC either toward or away from  
18 the geometrical center of the well. Our results revealed how various actin networks have  
19 distinct and specific impact on the distribution of pushing forces and confer some  
20 robustness to the mechanism of MTOC positioning by making it less sensitive to  
21 variations of MT length.

22

23

## 1 **Results**

### 2 **aMTOC positioning in microwells**

3 It is difficult to directly assess the mechanical effects of actin networks on the  
4 production of pushing forces by MTs in living cells because of the biochemical and  
5 structural complexities of cell interior, and the presence of motors exerting pulling forces  
6 on MTs. Therefore, to reconstitute the interaction of an aster of dynamic MTs with actin  
7 networks, we designed an *in vitro* reconstitution assay using purified proteins and  
8 microfabrication techniques.

9 We investigated how an astral array of MTs self-organizes in a cell-sized  
10 compartment. 3D microwell can be used to impose physical barrier to MT growth (Inoue  
11 *et al*, 2020; Laan *et al*, 2012). As compared to lipid droplets (Juniper *et al*, 2018; Pinot *et*  
12 *al*, 2009), microwells offer the possibility to control the size and shape of the container  
13 (Colin *et al*, 2020). Actual boundaries are made of lipids in living systems. Therefore, we  
14 started by setting up the coating of microwell with a lipid bilayer (Zieske & Schwille,  
15 2014) and further closed the upper surface of the container with a layer of mineral oil  
16 (Figure 1A-B, Appendix Fig. S1A-B). Lipids were properly diffusing in the bottom plane  
17 and the vertical edges of the microwell (Appendix Fig. S1C). However, there was a  
18 problem of tubulin precipitation, as reported previously (Weis *et al*, 2010; Baumann &  
19 Surrey, 2014). After 30 to 60 minutes of incubation of tubulin in the TicTac or the BRB80  
20 buffer, the tubulin precipitated (Appendix Fig. S2A) and microtubule dynamics stopped.  
21 A screening of the biochemical conditions (Appendix Fig. S2B-F) suggested that at lower  
22 temperature (22°C) and with high concentration of BSA and GTP, tubulin precipitation  
23 could be delayed, up to two hours (Figure 1C). As purified centrosomes generate a quite  
24 variable number of MTs (Inoue *et al*, 2019), we chose to work with artificial MTOCs  
25 (aMTOCs) made of short stabilized pieces of MTs grafted on a polystyrene bead (Figure  
26 1D). They efficiently generated 15 to 20 dynamic MTs per aMTOC (Figure EV1A-D).

27 We first analyzed the sensitivity of aMTOC positioning to the ratio of MT length  
28 over container length by varying tubulin concentrations in microwells of controlled size.  
29 As tubulin concentration has been increased from 14 to 26  $\mu\text{M}$ , the average length of MTs  
30 varied from 4 to 25  $\mu\text{m}$  (Figure 1E, F). The radius of the microwell was close to 19  $\mu\text{m}$ .  
31 Below 18  $\mu\text{M}$ , MTs were shorter than 10  $\mu\text{m}$  and aMTOC adopted a random position

1 (Figure 1G and Figure EV2A, B). At 18  $\mu\text{M}$  of tubulin, MTs were longer and could reach  
2 the microwell boundaries (Figure 1E, F, Figure EV2C and Movie EV1). In about 60 min  
3 (Figure 1H, I and Movie EV1), most aMTOC reached the center of the microwell and  
4 remained there (Figure 1G and Figure EV2B). Centering was also efficient at 22  $\mu\text{M}$  of  
5 tubulin (Figure 1G). At 26  $\mu\text{M}$  of tubulin, most MTs were longer than 20  $\mu\text{m}$  (Figure 1E).  
6 As they grew, they first ensured a proper centering but after an hour, MT elongation and  
7 slippage along microwell edges broke the network symmetry and MTs pushed aMTOC  
8 away from the center (Figure 1J, K, Figure EV2D and Movie EV2). Taken together, in our  
9 experimental system, aMTOC positioning appeared highly sensitive to the tubulin  
10 concentration and the MT length. Above a critical concentration of 22  $\mu\text{M}$ , MT elongation  
11 and reorientation could bias the distribution of pushing forces and promote aMTOC  
12 decentering, as previously described in water-in-oil droplets (Pinot *et al*, 2009).

13           Previous works based on numerical simulations suggested that the friction along  
14 the boundaries of the container might prevent the symmetry break by enforcing a vortex-  
15 like structure in the network that preserves MTOC centering (Letort *et al*, 2016). In cells,  
16 the actin filaments form distinct cortical and cytoplasmic networks that might restrict MT  
17 lateral translocation and aster displacement (Blanchoin *et al*, 2014; Field & Lénárt, 2011).  
18 Therefore, we tested how these various architectures might impact either centering or  
19 decentering mechanisms.

20

### 21 **Assembly of various actin architectures in microwells**

22           Rather than working with preassembled and stabilized actin filaments, we chose  
23 to grow actin filaments in the microwells in order to control their position and architecture  
24 by controlling the mechanism of actin network assembly. Unbranched actin network  
25 could be formed in the bulk of the microwell simply by spontaneously assembling 4  $\mu\text{M}$   
26 of actin monomers (Figure 2A, B and Appendix Fig. S3A). Alternatively, to limit the  
27 cytoplasmic pool, and favor the assembly of a dense cortical layer, actin filaments were  
28 nucleated near the lipid layer by a Nucleation Promoting Factor (NPF) attached to the  
29 lipid in the presence of the Arp2/3 complex and actin monomers in the solution (Figure  
30 2C, D and Appendix Fig. S3A, B).

1 We first tested the impact of these two actin architectures on aMTOC positioning  
2 independently of MTs (Figure 2E). Unbranched actin filaments in the bulk had no visible  
3 impact on bead position as compared to similar conditions without them (Figure 2E and  
4 Appendix Fig. S3C). Position of the beads was a bit centered in the presence of cortical  
5 actin, as the thickness of the cortical layer restricted the available space for beads (Figure  
6 2E and Appendix Fig. S3C, D).

7 These results showed that actin filaments in the bulk and branched cortical  
8 network can be reconstituted in 3D microwells and have distinct impact on aMTOC  
9 position independently of MTs. The two networks may also have specific effects on MT  
10 slippage or deformation and as such distinct impacts on the force distribution in the MT  
11 network and therefore on the positioning of the MTOC.

### 12 13 **Bulk actin network impairs aMTOC displacement and aster self-centering**

14 aMTOC displacements depend on the production of pushing forces by MT  
15 polymerization against container boundaries. However, the morphology of aster confers  
16 them a large effective cross-section that limits their displacements by viscous drag. We  
17 first tested whether the density of actin network in the bulk could impact the production  
18 of pushing forces against effective boundaries, reorganize the spatial distribution of MTs  
19 and thus affect the inner balance of force production by MT polymerization.

20 To test whether bulk actin network could impair the centering process, we  
21 worked in conditions where MT length was comparable to the microwell radius (ie at  
22  $18\mu\text{M}$  tubulin). aMTOC position was not dramatically affected by  $1\mu\text{M}$  of actin but  
23 appeared decentered with  $4\mu\text{M}$  of actin (Figure 3A, B-left and Figure EV3A). Indeed,  
24 time-lapse imaging revealed that aMTOC remained stuck at their initial position in the  
25 presence of  $4\mu\text{M}$  of actin (Figure 3C). The path-length of the MTOC was severely limited  
26 in the presence of  $4\mu\text{M}$  of actin, suggesting that the motion of the MTOC was restricted  
27 in the presence of actin filaments (Figure EV3B). Importantly, at this concentration,  
28 unbranched actin network had no impact on MT elongation (Figure 3D). In addition,  
29 higher concentrations of tubulin,  $26\mu\text{M}$ , although capable of promoting MT elongation,  
30 could not overcome aster immobilization by the bulk actin meshwork (Figure 3B-right  
31 and Figure EV3C). This suggested that the defective centering was due to friction

1 resisting aster displacement rather than steric effects blocking MT polymerization (Colin  
2 *et al*, 2018; Inoue *et al*, 2019). Indeed, implementing physical hindrance to aster  
3 displacement by taking into account steric effect of actin filaments along MT aster in  
4 numerical simulations was sufficient to account for the immobilization of MTOC by  
5 linear bulk actin filaments (Figure 3E-G, Figure EV3D-F and Movie EV3). Therefore,  
6 we conclude that the presence of a dense network of actin filaments in the bulk can affect  
7 MT aster centering by resisting aster translocation rather than impairing MT elongation.

8         These data also suggested that restricting the actin network to the periphery  
9 might specifically limit MT slippage without impairing aster translocation.

### 11 **Cortical branched actin meshwork favors aster centering**

12         To test whether cortical actin could counteract MT slippage and MTOC  
13 decentering, experiments were performed in the presence of long MTs (ie at 26 $\mu$ M  
14 tubulin) (Figure 4A). As described above, the cortical network clustered aMTOC in a  
15 smaller volume and thus induced a partial centering (Figure 2E-right, 4B-left).  
16 Interestingly, this centering was significantly improved by the growth of long MTs  
17 (Figure 4B-left and Figure EV4A). MT length was not significantly changed even in the  
18 absence or presence of cortical actin, suggesting that this effect is not due to interference  
19 of actin with MT elongation (Figure 4C). Instead, MTs appeared longer than the radius of  
20 the microwell and the network adopted a vortex-like structure (Figure 4D). Time-lapse  
21 imaging showed that in the absence of cortical actin, MTs were pivoting around the  
22 aMTOC, whereas they maintained their orientation and grew along the edge in the  
23 presence of cortical actin (Figure 4E-H, Figure EV7B-D and Movie EV4) The path-length  
24 of the MTOC was shortened in the presence of cortical actin, suggesting that the presence  
25 of cortical actin stabilized the position of the MTOC by restricting MT slippage (Figure  
26 EV4E). MT pivoting in the absence of cortical actin appeared associated with aMTOC  
27 decentering, whereas MT sneaking into the cortical actin was associated with aMTOC  
28 stable centering and maintenance at the center (Figure 4I, J). Numerical simulations in  
29 which friction was restricted to the cell periphery displayed similar aMTOC  
30 displacements and final positions (Figure 4K-M, Figure EV4F, G and Movie EV5),  
31 demonstrating that local steric interactions between cortical actin and MTs are indeed



1 sufficient to prevent MTOC decentering. From these results, we concluded that cortical  
2 actin network can counteract the effect of MT elongation and aster decentering by  
3 restricting MT slippage and thus maintaining a regular distribution of force application  
4 sites along the cortex and around the aMTOC. In addition, even at lower concentrations  
5 of tubulin (18  $\mu\text{M}$ ), MT asters displayed a proper centering mechanism in the presence of  
6 cortical actin (Figure 4B-right, and Figure EV4H). This showed that cortical actin can  
7 enforce a robust centering that is less sensitive to MT length. Importantly, cortical actin  
8 network of low density could not enforce MTOC centering, suggesting that resistance to  
9 MT slippage depends on actin network density (Figure EV4I, J).

10         These results also suggested that a heterogeneous pattern of cortical friction  
11 might create an asymmetry in the angular distributions of MTs, and an alignment of  
12 pushing forces leading to aMTOC decentering.

13

#### 14 **Asymmetric cortical actin meshwork induces aster decentering**

15         We reasoned that with lower actin filament density, which would be crosslinked  
16 to each other, we could enforce the asymmetry of the actin network growing from the  
17 walls of the microwells (Ierushalmi *et al*, 2020). Indeed, we found that with 0.5  $\mu\text{M}$   
18 instead of 2  $\mu\text{M}$  of actin and 100 nM of  $\alpha$ -actinin, the cortical network grew from all  
19 edges but formed an asymmetric cortex (Figure 5A and Figure EV5A, B). In cells, the  
20 inner region of the cytoplasm that is almost devoid of actin filament was defined as the  
21 actin inner zone (Figure EV5B) (Jimenez *et al*, 2021b). The growth of MTs from the  
22 asters did not seem to have an impact on the asymmetric architecture of the actin network  
23 (Figure 5B). To analyze aster positioning with respect to this asymmetry, images were  
24 reoriented in order to align horizontally the center of the actin inner zone and the center  
25 of the microwell (Figure 5C, D and Figure EV5C, D). To test the potential guiding effect  
26 of asymmetric cortical actin networks, we worked in decentering conditions, ie 26  $\mu\text{M}$   
27 tubulin, in which aMTOCs are randomly distributed in the microwell in the absence of  
28 actin (Figure 5E and Figure EV5E, F). By its thickness, the cortical actin network  
29 constrained asters positioning and limits aMTOC dispersion even in the absence of MTs  
30 (Figure 5F and Figure EV5E, F). However, as anticipated, the reorientation of the  
31 microwells with respect to the asymmetry of the actin network revealed that as MTs grew

1 from the asters they shifted the aMTOCs toward the center of the actin inner zone (Figure  
2 5G, H, I, Figure EV5E-G and Movie EV6). Interestingly, in conditions imposing shorter  
3 MTs and an efficient centering of the aster, ie  $18\mu\text{M}$  of tubulin, the asters in the presence  
4 of the asymmetric actin network appeared decentered toward the center of the actin inner  
5 zone as well (Figure 5J and Figure EV5G). Numerical simulations confirmed that a  
6 heterogeneous friction pattern due to variable thickness in the cortical actin network along  
7 microwell boundary was sufficient to push the MTOC away from the thicker actin layer  
8 and thus promote aster decentering (Figure 5K-M, Figure EV5H, I and Movie EV7).  
9 Overall, these results showed that the cortical actin network architecture can direct the  
10 position of MTOCs, either at the center or away from it, depending on its heterogeneity.  
11 It controls the force balance at the MTOC by modulating the pattern of friction resisting  
12 MT slippage and thus directing the localization of the sites of application of pushing  
13 forces.

14  
15  
16

## 1 **Discussion**

2           Our results suggest that actin networks make aster positioning both more robust  
3 and more versatile. Indeed, in the absence of actin filaments, asters displayed abrupt  
4 transitions from centering to decentering depending on MTs length. By contrast, bulk  
5 actin filaments resisted asters displacements and MTOC were hold in place,  
6 independently of the presence of MTs. Moreover, cortical actin networks specifically  
7 favored aster centering over a broad range of MT lengths. The presence of asymmetric  
8 actin resulted in decentering of the aster. From these observations, we propose that actin  
9 networks can modulate the sensitivity of MT aster positioning to variation of MT length.

10  
11           It has been reported that the presence of cytoplasmic actin network can affect  
12 MT organization (Dahlgaard *et al*, 2007; Field & Lénárt, 2011). The immobilization of  
13 MTOC by bulk actin filaments in our system is reminiscent of the regulation of MT aster  
14 in *Xenopus* extract and sea urchin embryo (Xie *et al*, 2022; Colin *et al*, 2018). Bulk actin  
15 network might resist the MTOC displacement by passive friction along the large cross-  
16 section area formed by radiating MTs. On the other hand, the robust polarization of MT  
17 network and decentering of MTOC by asymmetric organization of the cortical actin is  
18 reminiscent of various mechanism of mutual polarization of the actin and microtubule  
19 networks, such as ciliogenesis and immune synapse formation (Pitaval *et al*, 2017a;  
20 Stinchcombe & Griffiths, 2014b; Ritter *et al*, 2015) or MTOC positioning at the rear of  
21 migrating leukocytes (Kopf & Kiermaier, 2021; Mastrogiovanni *et al*, 2021). In these  
22 conditions, as in our reconstitution system, the actin network might control MTOC  
23 decentering by concentrating the distribution of the MT-based pushing forces in dense  
24 cortical regions. So our reconstitution assay based on a minimal set of components might  
25 properly account for the actual mechanism regulating MT aster positioning by pushing  
26 forces in living cells.

27           However, the conditions of our reconstitution assay did not include the key role  
28 played by molecular motors that move the MTOC by pulling on microtubules (Yi *et al*,  
29 2013) and by regulating their dynamics (Hooikaas *et al*, 2020) during cell polarization.  
30 Furthermore, our experimental conditions and the use of short pieces of MTs attached to  
31 a bead did not offer us the possibility to control MT pivoting around the aMTOC, a

1 property that could have promoted symmetry break and amplified MTOC decentering  
2 (Baumgärtner & Tolić, 2014; Fong *et al*, 2021; Letort *et al*, 2016). In addition, we studied  
3 aMTOC positioning in response to the production of pushing forces in cylindrical and  
4 rigid microwells. Softer materials would be necessary to study whether the forces  
5 produced by growing microtubules (Bornens *et al*, 1989; Fygenson *et al*, 1997) could  
6 deform the container, force microtubule relocalization, destabilize the central position,  
7 break network symmetry and promote MTOC decentering.

8

9 Building a synthetic cell from scratch is a powerful strategy to improve our  
10 understanding of cell biology, and pave the way toward new living materials (Salehi-  
11 Reyhani *et al*, 2017). Here, we established a way to combine dynamic MTs and actin  
12 filaments in cell-sized confinement. Our findings and techniques could be used as a step  
13 toward the reconstitution of the polarization process in synthetic cells.

14

## 1 **References**

- 2 Baumann H & Surrey T (2014) Motor-mediated cortical versus astral microtubule organization  
3 in lipid-monolayered droplets. *J Biol Chem* 289: 22524–22535
- 4 Baumgärtner S & Tolić IM (2014) Astral Microtubule Pivoting Promotes Their Search for  
5 Cortical Anchor Sites during Mitosis in Budding Yeast. *PLoS One* 9: e93781
- 6 Blanchoin L, Boujemaa-Paterski R, Sykes C & Plastino J (2014) Actin dynamics, architecture,  
7 and mechanics in cell motility. *Physiol Rev* 94: 235–263
- 8 Bornens M (2008) Organelle positioning and cell polarity. *Nat Rev Mol Cell Biol* 9: 874–886
- 9 Bornens M (2018) Cell polarity: having and making sense of direction—on the evolutionary  
10 significance of the primary cilium/centrosome organ in Metazoa. *Open Biol* 8
- 11 Bornens M, Paintrand M & Celati C (1989) The cortical microfilament system of lymphoblasts  
12 displays a periodic oscillatory activity in the absence of microtubules: implications for cell  
13 polarity. *J Cell Biol* 109: 1071–1083
- 14 Boujemaa-Paterski R, Suarez C, Klar T, Zhu J, Guérin C, Mogilner A, Théry M & Blanchoin L  
15 (2017) Network heterogeneity regulates steering in actin-based motility. *Nat Commun* 8:  
16 1–13
- 17 Brito DA, Strauss J, Magidson V, Tikhonenko I, Khodjakov A & Koonce MP (2005) Pushing  
18 forces drive the comet-like motility of microtubule arrays in Dictyostelium. *Mol Biol Cell*  
19 16: 3334–3340
- 20 Burakov A, Nadezhkina E, Slepchenko B & Rodionov V (2003) Centrosome positioning in  
21 interphase cells. *J Cell Biol* 162: 963–969
- 22 Burute M, Prioux M, Blin G, Truchet S, Letort G, Tseng Q, Bessy T, Lowell S, Young J, Filhol  
23 O, *et al* (2017) Polarity Reversal by Centrosome Repositioning Primes Cell Scattering  
24 during Epithelial-to-Mesenchymal Transition. *Dev Cell* 40: 168–184
- 25 Chevrier V, Piel M, Collomb N, Saoudi Y, Frank R, Paintrand M, Narumiya S, Bornens M &  
26 Job D (2002) The Rho-associated protein kinase p160ROCK is required for centrosome  
27 positioning. *J Cell Biol* 157: 807–817
- 28 Colin A, Singaravelu P, Théry M, Blanchoin L & Gueroui Z (2018) Actin-Network  
29 Architecture Regulates Microtubule Dynamics. *Curr Biol* 28: 2647-2656.e4
- 30 Colin L, Chevallier A, Tsugawa S, Gacon F, Godin C, Viasnoff V, Saunders TE & Hamant O  
31 (2020) Cortical tension overrides geometrical cues to orient microtubules in confined  
32 protoplasts. *Proc Natl Acad Sci U S A* 117: 32731–32738

- 1 Dahlggaard K, Raposo AASF, Niccoli T & St Johnston D (2007) Capu and Spire Assemble a  
2 Cytoplasmic Actin Mesh that Maintains Microtubule Organization in the Drosophila  
3 Oocyte. *Dev Cell* 13: 539–553
- 4 Dogterom M & Koenderink GH (2019) Actin–microtubule crosstalk in cell biology. *Nat Rev*  
5 *Mol Cell Biol* 20: 38–54
- 6 Dujardin DL, Barnhart LE, Stehman SA, Gomes ER, Gundersen GG & Vallee RB (2003) A  
7 role for cytoplasmic dynein and LIS1 in directed cell movement. *J Cell Biol* 163: 1205–  
8 1211
- 9 Elric J & Etienne-Manneville S (2014) Centrosome positioning in polarized cells: Common  
10 themes and variations. *Exp Cell Res* 328: 240–248
- 11 Ennomani H, Letort G, Guérin C, Martiel JL, Cao W, Nédélec F, De La Cruz EM, Théry M &  
12 Blanchoin L (2016) Architecture and Connectivity Govern Actin Network Contractility.  
13 *Curr Biol* 26: 616–626
- 14 Faivre-Moskalenko C & Dogterom M (2002) Dynamics of microtubule asters in  
15 microfabricated chambers: The role of catastrophes. *Proc Natl Acad Sci U S A* 99: 16788–  
16 16793
- 17 Farhadi L, Fermino Do Rosario C, Debold EP, Baskaran A & Ross JL (2018) Active Self-  
18 Organization of Actin-Microtubule Composite Self-Propelled Rods. *Front Phys* 0: 75
- 19 Field CM & Lénárt P (2011) Bulk cytoplasmic actin and its functions in meiosis and mitosis.  
20 *Curr Biol* 21: R825-30
- 21 Fong KK, Davis TN & Asbury CL (2021) Microtubule pivoting enables mitotic spindle  
22 assembly in *S. cerevisiae*. *J Cell Biol* 220
- 23 Fyngenson DK, Marko JF & Libchaber A (1997) Mechanics of microtubule-based membrane  
24 extension. *Phys Rev Lett* 79: 4497–4500
- 25 Hale CM, Chen WC, Khatau SB, Daniels BR, Lee JSH & Wirtz D (2011) SMRT analysis of  
26 MTOC and nuclear positioning reveals the role of EB1 and LIC1 in single-cell  
27 polarization. *J Cell Sci* 124: 4267–4285
- 28 Harris TJC, Sawyer JK & Peifer M (2009) How the cytoskeleton helps build the embryonic  
29 body plan: models of morphogenesis from *Drosophila*. *Curr Top Dev Biol* 89: 55–85
- 30 Holy TE, Dogterom M, Yurke B & Leibler S (1997) Assembly and positioning of microtubule  
31 asters in microfabricated chambers. *Proc Natl Acad Sci U S A* 94: 6228–6231

- 1 Hooikaas PJ, Damstra HG, Gros OJ, van Riel WE, Martin M, Smits YT, van Loosdregt J,  
2 Kapitein LC, Berger F & Akhmanova A (2020) Kinesin-4 KIF21B limits microtubule  
3 growth to allow rapid centrosome polarization in T cells. *Elife* 9
- 4 Hyman A, Drechsel D, Kellogg D, Salsler S, Sawin K, Steffen P, Wordeman L & Mitchison T  
5 (1991) Preparation of modified tubulins. *Methods Enzymol* 196: 478–485
- 6 Ierushalmi N, Malik-Garbi M, Manhart A, Shah EA, Goode BL, Mogilner A & Keren K (2020)  
7 Centering and symmetry breaking in confined contracting actomyosin networks. *Elife* 9
- 8 Inoue D, Kabir AMR, Tokuraku K, Sada K & Kakugo A (2020) Mechanical Stimulation-  
9 Induced Orientation of Gliding Microtubules in Confined Microwells. *Adv Mater*  
10 *Interfaces* 7: 1902013
- 11 Inoue D, Obino D, Pineau J, Farina F, Gaillard J, Guerin C, Blanchoin L, Lennon-Duménil A &  
12 Théry M (2019) Actin filaments regulate microtubule growth at the centrosome. *EMBO J*  
13 38
- 14 Jiang K, Toedt G, Montenegro Gouveia S, Davey NE, Hua S, Van Der Vaart B, Grigoriev I,  
15 Larsen J, Pedersen LB, Bezstarosti K, *et al* (2012) A proteome-wide screen for  
16 mammalian SxIP motif-containing microtubule plus-end tracking proteins. *Curr Biol* 22:  
17 1800–1807
- 18 Jimenez AJ, Schaeffer A, De Pascalis C, Letort G, Vianay B, Bornens M, Piel M, Blanchoin L  
19 & Théry M (2021a) Acto-myosin network geometry defines centrosome position. *Curr*  
20 *Biol* 31: 1206-1220.e5
- 21 Jimenez AJ, Schaeffer A, De Pascalis C, Letort G, Vianay B, Bornens M, Piel M, Blanchoin L  
22 & Théry M (2021b) Acto-myosin network geometry defines centrosome position. *Curr*  
23 *Biol* 31: 1206-1220.e5
- 24 Juniper MPN, Weiss M, Platzman I, Spatz JP & Surrey T (2018) Spherical network contraction  
25 forms microtubule asters in confinement. *Soft Matter* 14: 901–909
- 26 Kimura K & Kimura A (2011) Intracellular organelles mediate cytoplasmic pulling force for  
27 centrosome centration in the *Caenorhabditis elegans* early embryo. *Proc Natl Acad Sci U S*  
28 *A* 108: 137–142
- 29 Koonce MP, Köhler J, Neujahr R, Schwartz J-M, Tikhonenko I & Gerisch G (1999) Dynein  
30 motor regulation stabilizes interphase microtubule arrays and determines centrosome  
31 position. *EMBO J* 18: 6786–6792
- 32 Kopf A & Kiermaier E (2021) Dynamic Microtubule Arrays in Leukocytes and Their Role in  
33 Cell Migration and Immune Synapse Formation. *Front Cell Dev Biol* 9: 158

- 1 Laan L, Pavin N, Husson J, Romet-Lemonne G, Van Duijn M, López MP, Vale RD, Jülicher F,  
2 Reck-Peterson SL & Dogterom M (2012) Cortical dynein controls microtubule dynamics  
3 to generate pulling forces that position microtubule asters. *Cell* 148: 502–514
- 4 Letort G, Nedelec F, Blanchoin L & Théry M (2016) Centrosome centering and decentering by  
5 microtubule network rearrangement. *Mol Biol Cell* 27: 2833–2843
- 6 Letort G, Politi AZ, Ennomani H, Théry M, Nedelec F & Blanchoin L (2015) Geometrical and  
7 Mechanical Properties Control Actin Filament Organization. *PLOS Comput Biol* 11:  
8 e1004245
- 9 López MP, Huber F, Grigoriev I, Steinmetz MO, Akhmanova A, Koenderink GH & Dogterom  
10 M (2014) Actin-microtubule coordination at growing microtubule ends. *Nat Commun* 5
- 11 Ma R, Laan L, Dogterom M, Pavin N & Jülicher F (2014) General theory for the mechanics of  
12 confined microtubule asters. *New J Phys* 16: 013018
- 13 Mastrogiovanni M, Di Bartolo V & Alcover A (2021) Cell polarity regulators, multifunctional  
14 organizers of lymphocyte activation and function. *Biomed J*: 1–11
- 15 Meiring JCM, Shneyer BI & Akhmanova A (2020) Generation and regulation of microtubule  
16 network asymmetry to drive cell polarity. *Curr Opin Cell Biol* 62: 86–95
- 17 Nedelec F & Foethke D (2007) Collective Langevin dynamics of flexible cytoskeletal fibers.  
18 *New J Phys* 9: 427
- 19 Pavin N, Laan L, Ma R, Dogterom M & Jülicher F (2012) Positioning of microtubule  
20 organizing centers by cortical pushing and pulling forces. *New J Phys* 14: 105025
- 21 Pelletier JF, Field CM, Fürthauer S, Sonnett M & Mitchison TJ (2020) Co-movement of astral  
22 microtubules, organelles and F-actin by dynein and actomyosin forces in frog egg  
23 cytoplasm. *Elife* 9
- 24 Pinot M, Chesnel F, Kubiak JZ, Arnal I, Nedelec FJ & Gueroui Z (2009) Effects of  
25 Confinement on the Self-Organization of Microtubules and Motors. *Curr Biol* 19: 954–  
26 960
- 27 Pitaval A, Senger F, Letort G, Gidrol X, Guyon L, Sillibourne J & Théry M (2017a)  
28 Microtubule stabilization drives 3D centrosome migration to initiate primary ciliogenesis.  
29 *J Cell Biol* 216
- 30 Pitaval A, Senger F, Letort G, Gidrol X, Guyon L, Sillibourne J & Théry M (2017b)  
31 Microtubule stabilization drives 3D centrosome migration to initiate primary ciliogenesis.  
32 *J Cell Biol* 216: 3713–3728



1 Rickman J, Nédélec F & Surrey T (2019) Effects of spatial dimensionality and steric  
2 interactions on microtubule-motor self-organization. *Phys Biol* 16: 046004

3 Ritter ATT, Asano Y, Stinchcombe JC, Dieckmann NMGMG, Chen B-CC, Gawden-Bone C,  
4 van Engelenburg S, Legant W, Gao L, Davidson MWW, *et al* (2015) Actin Depletion  
5 Initiates Events Leading to Granule Secretion at the Immunological Synapse. *Immunity* 42:  
6 864–876

7 Salehi-Reyhani A, Ces O & Elani Y (2017) Artificial cell mimics as simplified models for the  
8 study of cell biology. *Exp Biol Med* 242: 1309–1317

9 Shao W, Yang J, He M, Yu XY, Lee CH, Yang Z, Joyner AL, Anderson K V., Zhang J, Tsou  
10 MFB, *et al* (2020) Centrosome anchoring regulates progenitor properties and cortical  
11 formation. *Nature* 580: 106–112

12 Shelanski ML (1973) Chemistry of the filaments and tubules of brain. *J Histochem Cytochem*  
13 21: 529–539

14 Stinchcombe JC & Griffiths GM (2014a) Communication, the centrosome and the  
15 immunological synapse. *Philos Trans R Soc B Biol Sci* 369

16 Stinchcombe JC & Griffiths GM (2014b) Communication, the centrosome and the  
17 immunological synapse. *Phil Trans R Soc* 369: 1–10

18 Tang N & Marshall WF (2012) Centrosome positioning in vertebrate development. *J Cell Sci*  
19 125: 4951–61

20 Vignaud T, Blanchoin L & Théry M (2012) Directed cytoskeleton self-organization. *Trends*  
21 *Cell Biol* 22: 671–682

22 Vladar EK, Bayly RD, Sangoram AM, Scott MP & Axelrod JD (2012) Microtubules Enable the  
23 Planar Cell Polarity of Airway Cilia. *Curr Biol* 22: 2203–2212

24 Weis F, Moullintraffort L, Heichette C, Chrétien D & Garnier C (2010) The 90-kDa heat shock  
25 protein Hsp90 protects tubulin against thermal denaturation. *J Biol Chem* 285: 9525–9534

26 Wu J, Misra G, Russell RJ, Ladd AJC, Lele TP & Dickinson RB (2011) Effects of dynein on  
27 microtubule mechanics and centrosome positioning. *Mol Biol Cell* 22: 4834–4841

28 Xie J, Najafi J, Le Borgne R, Verbavatz JM, Durieu C, Sallé J & Minc N (2022) Contribution of  
29 cytoplasm viscoelastic properties to mitotic spindle positioning. *Proc Natl Acad Sci U S A*  
30 119

31 Yi J, Wu X, Chung AH, Chen JK, Kapoor TM & Hammer JA (2013) Centrosome repositioning  
32 in T cells is biphasic and driven by microtubule end-on capture-shrinkage. *J Cell Biol* 202:  
33 779–792

- 1 Zhu J, Burakov A, Rodionov V & Mogilner A (2010) Finding the cell center by a balance of  
2 dynein and myosin pulling and microtubule pushing: A computational study. *Mol Biol Cell*  
3 21: 4418–4427
- 4 Zieske K & Schwille P (2014) Reconstitution of self-organizing protein gradients as spatial cues  
5 in cell-free systems. *Elife* 3  
6  
7

## 1 **Acknowledgements**

2 We thank Laura Schaedel for helping in the design and manufacturing of microwells and Gaelle  
3 Letort for advices and discussions about Cytosim. This work was supported by the European  
4 Research Council (Consolidator Grant 771599 (ICEBERG) to MT and Advanced Grant 741773  
5 (AAA) to LB). S.Y. was supported by fellowships from the EMBO (ALTF 652-2019), Astellas  
6 Foundation for research on metabolic disorders and Mochida memorial foundation for medical  
7 and pharmaceutical research. This work was also supported by the MuLife imaging facility, which  
8 is funded by GRAL, a program from the Chemistry Biology Health Graduate School of University  
9 Grenoble Alpes (ANR-17-EURE-0003).

10

## 11 **Disclosure and competing interests statement**

12 The authors declare that they have no conflict of interest.

13

14

## 15 **Materials and Methods**

### 16 **Protein expression and purification**

17 Tubulin was purified from fresh bovine brain by three cycles of temperature-dependent  
18 assembly/disassembly in Brinkley Buffer 80 (BRB80: 80 mM Pipes pH 6.8, 1 mM EGTA and  
19 1 mM MgCl<sub>2</sub>) (Shelanski, 1973). MAP-free tubulin was purified by cation-  
20 exchange chromatography (EMD SO, 650 M, Merck) in 50 mM Pipes, pH 6.8,  
21 supplemented with 0.2 mM MgCl<sub>2</sub>, and 1 mM EGTA. Fluorescently labelled tubulin (ATTO-  
22 488- or ATTO-647-labelled) and biotinylated tubulin were prepared by following previously  
23 published method (Hyman *et al*, 1991). Actin was purified from rabbit skeletal-muscle acetone  
24 powder. Monomeric Ca-ATP-actin was purified by gel-filtration chromatography  
25 on Sephacryl S-300 at 4°C in G buffer (2 mM Tris-HCl, pH 8.0, 0.2 mM ATP, 0.1 mM  
26 CaCl<sub>2</sub>, 1 mM NaN, and 0.5 mM dithiothreitol (DTT)). Actin was labelled on lysines with Alexa-  
27 568. The Arp2/3 complex, recombinant GST- $\alpha$ -actinin 4 and GST-WA (a truncated version of  
28 human WASP) were purified in accordance with previous methods (Ennomani *et al*, 2016;  
29 Boujemaa-Paterski *et al*, 2017).  
30 Snap-Streptavidin-WA (pETplasmid) was expressed in Rosettas 2 (DE3) pLysS (Merck, 71403).  
31 Culture was grown in TB medium supplemented with 30  $\mu$ g/mL kanamycine and 34  $\mu$ g/mL  
32 chloramphenicol, then 0.5 mM isopropyl  $\beta$ -D-1- thiogalactopyranoside (IPTG) was added and  
33 protein was expressed overnight at 16 °C. Pelleted cells were resuspended in Lysis buffer (20 mM  
34 Tris pH8, 500 mM NaCl, 1 mM EDTA, 15 mM Imidazole, 0,1% TritonX100, 5% Glycerol, 1  
35 mM DTT). Following sonication and centrifugation, the clarified extract was loaded on a Ni

1 Sepharose high performance column (GE Healthcare Life Sciences, ref 17526802). Resin was  
2 washed with Wash buffer (20 mM Tris pH8, 500 mM NaCl, 1 mM EDTA, 30 mM Imidazole, 1  
3 mM DTT). Protein was eluted with Elution buffer (20 mM Tris pH8, 500 mM NaCl, 1 mM EDTA,  
4 300 mM Imidazole, 1 mM DTT). Purified protein was dialyzed overnight 4°C with storage buffer  
5 (20 mM Tris pH8, 150 mM NaCl, 1 mM EDTA, 1 mM DTT), concentrated with Amicon 3KD  
6 (Merck, ref UFC900324). Aliquots were flash frozen in liquid nitrogen and stored at -80 °C.

### 9 **Preparation of an artificial MTOC**

10 To prepare microtubule seeds, the mixture containing 3 μM of fluorescent-labeled tubulin, 7 μM  
11 of biotinylated tubulin and 0.5 mM GMPCPP (Jena Bioscience, NU-405S) in BRB80 buffer was  
12 incubated at 37°C for 40 min. After the incubation, 10 μM of Taxol was added and the mixture  
13 was incubated at room temperature for 10 min. The microtubule seeds were then pelleted by  
14 centrifugation at 20,238 x g for 10 min and were resuspended in the BRB80 supplemented with  
15 0.5 mM GMPCPP and 10 μM Taxol. The seeds were flash frozen and stored in liquid nitrogen.

16 To prepare the Neutravidin-coated beads, the polystyrene beads containing surface primary amino  
17 groups (PolySciences, 17145-5, Diameter 3 μm) were incubated with 10 mM of Sulfo-NHS-LC-  
18 LC-Biotin (ThermoFisher, 21338) at room temperature for 40 min to modify their surface with  
19 biotin. The beads were washed with phosphate buffered saline (PBS) and then with HKEM buffer  
20 (10 mM HEPES (pH 7.5), 50 mM KCl, 5 mM MgCl<sub>2</sub>, 1 mM EGTA) supplemented with 0.1%  
21 bovine serum albumin (BSA). The beads were incubated with 1 mg/mL of  
22 Neutravidin (ThermoFisher, 31000) at 15°C for 30 min or at 4°C for 2 hours. After washing the  
23 beads with HKEM buffer supplemented with 0.1% BSA, the beads were resuspended in 200 μL  
24 of HKEM buffer supplemented with 0.1% BSA. The beads solution was then mixed with 10 μL  
25 of the microtubule seeds. The mixture was incubated under rotation at room temperature  
26 overnight. Before mixing the aMTOCs (microtubule seeds + beads) with the reaction mixture  
27 containing free tubulin, the solution containing aMTOCs was washed with HKEM supplemented  
28 with 0.1% BSA to remove excess seeds and Taxol.

### 30 **Preparation of small unilamellar vesicles (SUV)**

31 L-α-phosphatidylcholine (EggPC) (Avanti, 840051C), 1,2-distearoyl-sn-glycero-  
32 3 phosphoethanolamine-N-[biotinyl(polyethylene glycol)-2000] (DSPE-PEG(2000)-Biotin)  
33 (Avanti, 880129C) and ATTO 647N labeled DOPE (ATTO-TEC, AD 647N-161 dehydrated)  
34 were used. Lipids were mixed in glass tubes as follows: Type 1 (99% EggPC (10 mg/mL) and 1%  
35 DOPE-ATTO390 (1 mg/mL)), Type 2 (98.75% EggPC (10 mg/mL) and 0.25% DSPE-PEG-  
36 Biotin (10 mg/mL) and 1% DOPE-ATTO390 (1 mg/mL)), Type 3 (99.5% EggPC (10 mg/mL),

1 0.25% DSPE-PEG-Biotin (10 mg/mL) and 0.25% DOPE-ATTO647N (1 mg/mL)). The mixture  
2 was dried with nitrogen gas. The dried lipids were incubated in a vacuum overnight. After that,  
3 the lipids were hydrated in the SUV buffer (10 mM Tris (pH 7.4), 150 mM NaCl, 2 mM  
4 CaCl<sub>2</sub>). The mixture was sonicated on ice. The mixture was then centrifuged for 10 min at 20,238  
5 x g to remove large structures. The supernatants were collected and stored at 4°C. The final  
6 concentration of lipids was adjusted to 0.5 mg/mL. The Type 2 SUV was used to bind snap-  
7 streptavidin-WA onto the lipid layer. The Type 3 SUV was used to visualize lipids on microwells.  
8 In other experiments, the Type 1 SUV was used.

### 9 10 **Construction of microwells**

11 The master mold (approximately 20 μm of thickness) was fabricated through photolithography  
12 using SU8 3025 (MicroChem) and then vapor silanized with Trichloro (1H,1H,2H,2H-perfluoro-  
13 octyl) silane (Sigma, 448931). To make 1st PDMS, the mixture of prepolymer and curing agent  
14 (Dow, SYLGARD 184 silicone elastomer kit) was poured onto the master mold. It was  
15 baked at 70°C for 2 hours. The 1st PDMS was then vapor silanized  
16 with Trichloro (1H,1H,2H,2H-perfluoro-octyl) silane. The 2nd PDMS was made from the  
17 silanized 1st PDMS as a template. The 2nd PDMS was cut into small pieces and used as PDMS  
18 stamps.

19 Glasses were cleaned by successive chemical treatments: 30 min in acetone with sonication, 15  
20 min in ethanol (96%), washing ultrapure water, 2 hours in HellmanexIII (2% in water, Hellma),  
21 washing in ultrapure water. The glasses were then dried. The slide glasses were oxidized in plasma  
22 cleaner (Diener) for 2 min at 80% power and then incubated overnight in a solution of 1 mg/mL  
23 of mPEG-Silane (30kDa, PSB-2014, Creative PEG works), 96% ethanol and 0.1%(v/v) HCl. The  
24 slide glasses were then dried and stored at 4°C.

25 To make microwell chip on a cover glass, the PDMS stamp was placed on the cleaned cover glass  
26 (20 mm x 20 mm, No.1), facing the pillar surface of the stamp onto the glass. NOA81(Norland  
27 Products) drop was put at the side of the PDMS stamp to fill the space between the PDMS pillars  
28 with NOA81. The NOA81 was cured with UV light (UVKUB2, 100%, 12 min). The PDMS  
29 stamp and excess NOA81 were then removed.

### 30 31 **Sample preparation**

32 To make a reaction chamber, a cover glass with microwell chip was first oxidized in plasma  
33 cleaner (diener) for 2 min at power of 80%. The cover glass with microwell chip was attached  
34 onto the silane-PEG coated slide glass with two double-sided tapes (70 μm thickness), facing the  
35 side of microwell chip to the slide glass. The SUV solution (0.5 mg/mL) was introduced into the  
36 chamber and incubated for 10 min to make a supported lipid bilayer on the surface of microwell

1 chip. It was washed with the SUV buffer to remove excess SUV and then washed with HKEM  
2 buffer supplemented with 0.1% BSA. Unless otherwise noted, microtubule and actin assembly  
3 were induced by diluting tubulin dimers (20% labelled) and/or actin monomers (10% labelled) in  
4 the reaction mixture containing the TicTac buffer (10 mM Hepes, 16 mM Pipes (pH 6.8), 50  
5 mM KCl, 1 mM EGTA, 5 mM MgCl<sub>2</sub>) supplemented with 5% BSA, 4.4 mM GTP, 2.7 mM ATP,  
6 20 mM DTT, 20 µg/mL catalase, 3 mg/mL glucose, 100 µg/mL glucose oxidase. Microtubule  
7 aster formation was induced by adding microtubule seeds coated beads (aMTOCs) into the  
8 mixture.

9 To induce branched actin assembly from the edge of microwells, the SUV solution containing  
10 DSPE-PEG-Biotin (Type 2 SUV) was used for lipid coating. Before introducing the reaction  
11 mixture into the chamber, HKEM buffer containing 200 nM of snap-streptavidin-WA (used  
12 as an NPF) and 0.1% BSA was loaded into the chamber and incubated for 5 min. The excess WA  
13 was then removed by perfusing HKEM buffer supplemented with 0.1% BSA. 80 nM of the  
14 Arp2/3 complex was added in the reaction mixture. To make asymmetric cortical actin structures,  
15 100 nM of GST- $\alpha$ -actinin 4 was also added.

16 The reaction mixture was introduced into the chamber immediately after the preparation of the  
17 mixture. Mineral oil (Paragon Scientific, RTM13) was then loaded into the chamber in order to  
18 close the wells. Unless otherwise noted, the chamber was incubated at room temperature (22-  
19 23°C) in order to prevent tubulin precipitation. The final position of the aMTOCs was analyzed  
20 at 2 hours after sample preparation. Experiments were repeated to confirm the reproducibility.

21 For initial screening of biochemical conditions (in Figure 1C and Appendix Fig.  
22 S2), TicTac buffer supplemented with 0.1% BSA, 1 mM GTP, 2.7 mM ATP, 20 mM DTT,  
23 20 µg/mL catalase, 3 mg/mL glucose, 100 µg/mL glucose oxidase was used as a control buffer  
24 solution. BSA (Sigma, A7030), Polyethylene Glycol (PEG) 3k (Sigma, P3640), PEG 20k (Sigma,  
25 95172), Glycerol (CARLO ERBA), Ficoll400 (Sigma, F9378) and Dextran 40k (Sigma, 31389)  
26 were added in the solution at the indicated concentrations. The samples were incubated at the  
27 indicated temperatures.

28

## 29 **Microscopy**

30 Microtubule asters and actin filaments in microwells were visualized using a confocal spinning-  
31 disc system (EclipseTi-E Nikon inverted microscope equipped with a CSUX1-A1 Yokogawa  
32 confocal head, an Evolve EMCCD camera (Photometrics), a Nikon CFI Plan-Apo  $\times$ 60 NA1.4 oil  
33 immersion objective, a Nikon CFI S-Fluor  $\times$ 100 NA1.30 oil immersion objective and a Nikon  
34  $\times$ 20 NA0.75 dry objective). Time-lapse imaging was performed using Metamorph software  
35 (Universal Imaging). For time-lapse imaging of microtubule asters in microwells, images were

1 taken every 5 or 10 min to avoid photo-damages of microtubules. Photo-bleaching experiments  
2 of lipids were also performed on this system using an iLas<sup>2</sup> device.

3 To measure the position of aMTOC in microwells, the images were acquired using an  
4 upright Axioimager M2 Zeiss microscope equipped with an EC Plan-Neofluar dry ×20 NA0.5 dry  
5 objective and CoolSNAP EZ camera (Photometrics) or using the confocal spinning-disk system  
6 described above.

7 To visualize individual microtubules and actin filaments, an objective-based total internal  
8 reflection fluorescence (TIRF) microscopy instrument composed of a Nikon Eclipse Ti, an  
9 azimuthal iLas<sup>2</sup> TIRF illuminator (Roper Scientific), a ×60 NA1.49 TIRF objective lens, a x100  
10 NA1.49 TIRF objective lens and an Evolve EMCCD camera (Photometrics) was used. This  
11 system was also used to visualize tubulin precipitation in microwells. Excitation was achieved  
12 using 491, 561 and 642 nm lasers.

13

#### 14 **Image processing and measurements**

15 To visualize microtubule asters in microwells, the images were processed to improve the signal-  
16 to-noise ratio. Background subtraction was performed using Fiji (NIH). To further improve the  
17 signal-to-noise ratio, deconvolution was also performed for some of the images (Figure 1F, 3D  
18 and 4D) using DeconvolutionLab2 in Fiji before background  
19 subtraction. Background subtraction was not performed to show free tubulin signals in Figure 1C  
20 and Appendix Fig. S2A-E. Maximum projection was performed to show microtubule asters using  
21 Fiji. To visualize actin networks along the vertical edges, maximum projection was performed  
22 excluding the bottom and the top images of microwells (partial maximum  
23 projection). Microtubule length was manually measured using a 3D distance measurement tool in  
24 Fiji. Kymograph and temporal-color coded images were generated using plugins in Fiji. The  
25 orientation of MTs was measured and visualized using OrientationJ in Fiji. The orientation was  
26 evaluated for every pixel and the histogram was weighted by the coherency parameter.

27 Measurement of the center (centroid) of wells and the center of aMTOCs was performed using  
28 Fiji with bright-field images. Microwells containing only a single aMTOC were analyzed.  
29 Distance from the aMTOC to center of the well was measured from each XY coordinates. The  
30 actin inner zone (AIZ) was determined by setting thresholds of the fluorescence signals of actin.  
31 Then, the center of the AIZ was measured. The angles of the aMTOC and the center of the AIZ  
32 relative to the well center were calculated from each XY coordinate. To analyze aMTOC  
33 positioning relative to the center of the AIZ, wells were reoriented based on each XY coordinates  
34 in order to align the angles from the well center to center of the AIZ (See also ).

35

#### 36 **Numerical simulations**

1 Simulations were performed using Cytosim software (Nedelec & Foethke, 2007). The motion of  
2 elastic filaments and solids surrounded by a viscous fluid was calculated using Langevin  
3 dynamics (Nedelec & Foethke, 2007). The main parameters used in the simulation were presented  
4 in Appendix Table S1.

5 In the simulations, repulsive steric effects between actin filaments and microtubule aster were  
6 considered. As a limitation in the simulation, steric repulsion also occurs between actin filaments  
7 and between microtubules at the same steric force. Attractive steric forces between filaments  
8 were not included in the simulations. The steric parameters were adapted from the range in  
9 previous studies testing steric interactions between microtubules or actin filaments using Cytosim  
10 (Letort *et al*, 2015; Rickman *et al*, 2019). Because of excessive computational costs, it was  
11 difficult to perform simulations of centrosome positioning with dense actin filaments. Therefore,  
12 to reduce computational costs, the effective diameter of microtubules and actin filaments was set  
13 to 100 nm (Rickman *et al*, 2019; Letort *et al*, 2015) and the cell size was set to 10  $\mu\text{m}$  in radius. In  
14 addition, the total time simulated was set to 150 to 250 seconds. The simulations were performed  
15 in the two-dimensional mode.

16 Bulk actin network was made by adding actin filaments in the cell without fixation of their  
17 position. To make actin meshwork near the cell periphery, the actin nucleation factors and  
18 branching factors were positioned near the cell periphery (within 7 to 9.2  $\mu\text{m}$  from the cell  
19 center). The position of actin nucleation factors was fixed, so that the position of one of the ends  
20 of actin filaments was fixed at the initial position. When the actin branching factor binds to an  
21 existing actin filament, it nucleates a new actin filament from the existing filament. Asymmetric  
22 actin network was made by asymmetrically localizing the actin nucleation factors and the actin  
23 branching factors.

24

## 25 **Statistics**

26 Statistical tests were performed using R statistical software. Statistical test, sample sizes and P  
27 values are described in each figure legend.

28

## 29 **Data availability**

30 This study includes no data deposited in external repositories. The data that support the findings  
31 of this study are available from the corresponding author upon request.

32

33



1 **Figure legends**

2

3 **Figure 1. aMTOC positioning in microwells.**

4 **(A)** Scheme of microwells (See also Appendix Fig. S1A, B).

5 **(B)** Images of fluorescence-labelled lipid. XY and XZ view of microwells were shown.

6 **(C)** A screening of biochemical conditions to slow down tubulin precipitation (See also Appendix  
7 Fig. S2 and Methods).

8 **(D)** Scheme of preparation of an artificial MTOC (aMTOC). Biotinylated MT seeds were attached  
9 on NeutrAvidin-coated beads. By the addition of free tubulin, MT polymerization occurs from  
10 the beads (See also Methods).

11 **(E)** MT length at the indicated tubulin concentrations in microwells. (Tubulin 14  $\mu\text{M}$  n = 71,  
12 18  $\mu\text{M}$  n = 134, 26  $\mu\text{M}$  n = 97 MTs (8 wells, respectively)) \*\*\*\*p<0.0001 (Kruskal-Wallis test  
13 with Dunn's multiple comparison test).

14 **(F)** Representative images of MT asters with various tubulin concentrations. Images were taken  
15 at 2 hours after sample preparation.

16 **(G)** Distance from aMTOC to center of the well at the indicated tubulin concentrations (2 hours  
17 after sample preparation). (Tubulin 0  $\mu\text{M}$  n = 62, 10  $\mu\text{M}$  n = 59, 14  $\mu\text{M}$  n = 60, 18  $\mu\text{M}$  n = 68,  
18 22  $\mu\text{M}$  n = 60, 26  $\mu\text{M}$  n = 65 wells) \*\*p<0.01, \*\*\*\*p<0.0001, ns (not significant)>0.1 (Kruskal-  
19 Wallis test with Dunn's multiple comparison test).

20 **(H)** Time-lapse imaging of MT aster formation at 18  $\mu\text{M}$  of tubulin.

21 **(I)** aMTOC position over time at 18  $\mu\text{M}$  of tubulin. Bright-field images were taken at 1 min  
22 intervals. Positions of 10 individual aMTOCs were shown with different colors.

23 **(J)** Time-lapse imaging of MT aster formation at 26  $\mu\text{M}$  of tubulin.

24 **(K)** aMTOC position over time at 26  $\mu\text{M}$  of tubulin. Bright-field images were taken at 1 min  
25 intervals. Positions of 10 individual aMTOCs were shown with different colors.

26 Data information: Scale bar 10  $\mu\text{m}$ . Violin plots were shown with the median (horizontal line).

27

28 **Figure 2. Assembly of various actin architectures in microwells.**

29 **(A, B)** Unbranched, bulk actin network. XY and XZ views were shown. Higher magnification  
30 image (XY view) was shown in **(B)**.

31 **(C, D)** Cortical branched actin network. XY and XZ views were shown. NPF (streptavidin-tagged  
32 WA) was coated on the lipid-biotin. Higher magnification image (XY view) was shown in **(D)**.

33 **(E)** aMTOC position in the absence of free tubulin. Left, representative images showing actin and  
34 the aMTOCs in microwells. Right, measurement of distance from aMTOC to center of the well  
35 (2 hours after sample preparation). Violin plots were shown with the median (horizontal  
36 line). (Actin 0  $\mu\text{M}$  n = 60, Actin 4  $\mu\text{M}$  Bulk n = 60, Actin 4  $\mu\text{M}$  Cortex n = 63

1 wells) \*\*\*\* $p < 0.0001$ , ns (not significant) $> 0.1$  (Kruskal-Wallis test with Dunn's multiple  
2 comparison test).

3 Data information: Scale bar 10  $\mu\text{m}$ .

4

5 **Figure 3. Bulk actin network impairs aMTOC displacement and aster self-centering.**

6 **(A)** Representative image of MT aster in the presence of bulk actin network. Tubulin 18  $\mu\text{M}$  and  
7 actin 4  $\mu\text{M}$ .

8 **(B)** Distance from aMTOC to well center (2 hours after sample preparation). Left: Tubulin  
9 18  $\mu\text{M}$ . (Actin 0  $\mu\text{M}$   $n = 68$ , 1  $\mu\text{M}$   $n = 65$ , 4  $\mu\text{M}$   $n = 71$  wells). Right: Tubulin 26  $\mu\text{M}$  Actin 4  $\mu\text{M}$   
10 ( $n = 66$  wells). \*\*\*\* $p < 0.0001$ , ns (not significant) $> 0.1$  (Kruskal-Wallis test with Dunn's multiple  
11 comparison test).

12 **(C)** aMTOC position over time. Tubulin 18  $\mu\text{M}$  and Actin 4  $\mu\text{M}$ . Bright-field images were taken  
13 at 1 min intervals. Positions of 10 individual aMTOC were shown with different colors.

14 **(D)** Measurement of MT length in the absence or presence of bulk actin network. Tubulin 18  $\mu\text{M}$ .  
15 Images were taken 2 hours after sample preparation. (Actin 0  $\mu\text{M}$   $n = 109$ , 4  $\mu\text{M}$   $n = 118$  MTs  
16 (from 8 wells, respectively)). ns (not significant) $> 0.1$  (Mann-Whitney U test).

17 **(E)** Simulations in the absence (top) or presence (bottom) of actin filaments. Different time points  
18 (From left, 25, 100 and 150 sec) were shown. MTOC, gray, MT, black, Actin, pink.

19 **(F)** Trajectories of MTOCs from blue (0 sec) to red (150 sec). 15 simulations per condition. The  
20 initial position (0 sec) was randomly chosen.

21 **(G)** Final position of MTOC (at 150 sec). 15 simulations per condition. \*\*\*\* $p < 0.0001$  (Mann-  
22 Whitney U test).

23 Data information: Violin plots were shown with the median (horizontal line). Scale bar 10  $\mu\text{m}$  in  
24 (A), (C) and (D).

25

26 **Figure 4. Cortical branched actin meshwork favors aster centering.**

27 **(A)** Representative image of MT aster with cortical actin. Partial maximum projection was  
28 shown. Tubulin 26  $\mu\text{M}$ , actin 2  $\mu\text{M}$  and Arp2/3 complex were added into NPF (WA) coated  
29 microwells.

30 **(B)** Distance from aMTOC to well center (2 hours after sample preparation). Left: Tubulin 26  $\mu\text{M}$   
31 Actin 0  $\mu\text{M}$   $n = 61$ , Tubulin 0  $\mu\text{M}$  Actin 2  $\mu\text{M}$   $n = 73$ , Tubulin 26  $\mu\text{M}$  Actin 2  $\mu\text{M}$   $n = 70$  wells.  
32 Tubulin 18  $\mu\text{M}$  Actin 2  $\mu\text{M}$   $n = 76$  wells. \*\* $p < 0.01$ , \*\*\*\* $p < 0.0001$ , ns (not significant) $> 0.1$   
33 (Kruskal-Wallis test with Dunn's multiple comparison test).

34 **(C)** Measurement of MT length in the absence or presence of cortical actin. Tubulin 26  $\mu\text{M}$ .  
35 Images were taken 2 hours after sample preparation. (Actin 0  $\mu\text{M}$   $n = 96$ , 2  $\mu\text{M}$  cortex  $n = 104$   
36 MTs (from 6 wells, respectively)). ns (not significant) $> 0.1$  (Mann-Whitney U test).

1 **(D)** Representative images of MT organization in the absence or presence of cortical actin.  
2 Tubulin 26  $\mu\text{M}$ .  
3 **(E, F)** Time-lapse imaging of MT aster positioning at 26  $\mu\text{M}$  in the absence **(E)** or presence **(F)**  
4 of cortical actin. Final actin structure was shown in **(A)**. Magnified images were also shown. In  
5 magnified images in **(E)**, the blue and yellow arrowheads indicate the MTs slipping along the well  
6 edge, respectively. Right schemes indicate how MTs behave along cell boundary. In the absence  
7 of actin, MTs slipped and reoriented along well boundary as they grew. In contrast, MT  
8 reorientation was restricted in the presence of actin, although MTs can grow through actin  
9 network and along well boundary.  
10 **(G)** Orientation of MTs near the well edge in the absence or presence of cortical actin. Orientation  
11 of MTs were shown with different colors. Right graph indicates the measurement of the MT  
12 orientation using Orientation J. The different time points were shown with different colors.  
13 Another example was also shown in Figure EV4D. In the absence of cortical actin, the MT  
14 orientation dynamically changed over time, whereas in the presence of cortical actin, the MT  
15 orientation was not significantly changes.  
16 **(H)** MT motion around the aMTOC shown in **(E)** and **(F)**. Temporal-color coded images were  
17 shown. The position of aMTOC was centered at each time point in the image.  
18 **(I)** aMTOC position overtime in the absence (left) or presence (right) of cortical actin. 5  
19 representative data per condition were shown.  
20 **(J)** Representative trajectories of aMTOCs in microwells from light colors (0 min) to dark colors  
21 (120 min). Time-lapse imaging was performed for 2 hours at 10 min intervals. 3 trajectories per  
22 condition were shown with different colors.  
23 **(K)** Simulations in the absence or presence of actin. Different time points (From left, 25, 75, 150  
24 and 200 sec) were shown. MTOC, gray, MT, black, Actin, pink.  
25 **(L)** Representative trajectories of MTOC from blue (0 sec) to red (200 sec). The initial position  
26 (0 sec) was randomly chosen within 4  $\mu\text{m}$  from the cell center. 3 simulations per condition.  
27 **(M)** Final position of MTOC (at 200 sec). 15 simulations per condition. \*\*\*\* $p < 0.0001$  (Mann-  
28 Whitney U test).  
29 Data information: Violin plots were shown with the median (horizontal line). Scale bar 10  $\mu\text{m}$  in  
30 **(A)** and **(D)**-**(H)**.

31

32 **Figure 5. Asymmetric cortical actin meshwork induces aster decentering.**

33 **(A)** Representative image of asymmetric actin cortex. Actin 0.5  $\mu\text{M}$ ,  $\alpha$ -actinin 100 nM and  
34 Arp2/3 complex were added into NPF (WA) coated microwells. In the right image, the center of  
35 the well and the center of the actin inner zone were indicated. A single slice of the image was  
36 shown. Scale bar left 50  $\mu\text{m}$ , right 10  $\mu\text{m}$ .

1 **(B)** Distance between well center and center of the actin inner zone. (Tubulin 0  $\mu\text{M}$   $n = 74$ , 26  $\mu\text{M}$   
2  $n = 79$  wells) ns (not significant) $>0.1$  (Mann-Whitney U test).

3 **(C)** Representative image of MT aster with asymmetric actin. Tubulin 26  $\mu\text{M}$ . Partial maximum  
4 projection was shown.

5 **(D)** Scheme of angle measurements. Angles from the well center to the aMTOC and the center of  
6 the actin inner zone were measured. In (F), (I) and (J), the wells were reoriented based on each  
7 XY coordinates in order to align the angles from well center to center of the actin inner zone  
8 at  $0^\circ$  (See also Figure EV5C-D).

9 **(E, F)** Distributions of aMTOCs. Left, aMTOC positions ( $\mu\text{m}$ ) relative to well center. Right,  
10 Angular distributions (%) of aMTOCs from well center. (Tubulin 26  $\mu\text{M}$  Actin 0  $\mu\text{M}$   $n = 65$ ,  
11 Tubulin 0  $\mu\text{M}$  Actin 0.5  $\mu\text{M}$   $n = 74$ ) Blue and red dots indicate the position of aMTOC and the  
12 center of the actin inner zone after alignment, respectively.

13 **(G)** Time-lapse imaging of MT aster in the presence of asymmetric actin. Tubulin 26  $\mu\text{M}$ . In  
14 magnified images, the arrow head indicate the MT slipping along the well edge and the orange  
15 dot indicate the MT hitting the well edge.

16 **(H)** Actin network structure of (H) at the initial (0 min) and final time point (120 min). Partial  
17 maximum projection was shown.

18 **(I, J)** Distributions of aMTOCs. Left, aMTOC positions ( $\mu\text{m}$ ) relative to well center. Right,  
19 Angular distributions (%) of aMTOCs from well center. (Tubulin 26  $\mu\text{M}$  Actin 0.5  $\mu\text{M}$   $n = 79$   
20 wells, Tubulin 18  $\mu\text{M}$  Actin 0.5  $\mu\text{M}$   $n = 68$  wells) Blue and red dots indicate the position of  
21 aMTOC and the center of the actin inner zone after alignment, respectively.

22 **(K)** Simulations in the absence (top) or presence (bottom) of asymmetric actin (See also Figure  
23 EV5H). Initial position was set to the cell center. Time point: 25, 75, 150 and 250 sec. MTOC,  
24 gray, MT, black, Actin, pink.

25 **(L)** Trajectories of MTOCs from blue (0 sec) to red (250 sec). 20 simulations. Initial position:  
26 cell center.

27 **(M)** Final position of MTOC along X-axis (at 250 sec). 0 indicates the center along X axis in cells.  
28 20 simulations per condition.  $*p < 0.1$  (Mann-Whitney U test).

29 Data information: Violin plots were shown with the median (horizontal line). Scale bar, 10  $\mu\text{m}$  in  
30 (C), (G) and (H).

1

2 **Figure EV1. Characterization of an artificial MTOC.**

3 (A) Observation of MT aster formation using TIRF microscope. Scale bar 10  $\mu\text{m}$ .

4 (B) Time-lapse imaging of the MT aster formation using TIRF. Scale bar 10  $\mu\text{m}$ .

5 (C) Magnified images of (B). Time-interval 30 sec. Time bar indicates (min:sec). MTs showing  
6 dynamic instability were indicated with asterisks. Scale bar 5  $\mu\text{m}$ .

7 (D) Number of MTs emanating from the aMTOCs in microwells. Tubulin 18  $\mu\text{M}$ . n = 20  
8 wells. Violin plots were shown with the median (horizontal line).

9

10 **Figure EV2. Characterization of aMTOC positioning in microwells.**

11 (A) Consideration of the probability of aMTOC distribution. When the volumes of 6 segments  
12 (equal intervals from well center) are considered as shown in the left scheme, the volume per  
13 segment increases from well center toward well edge (left histogram), suggesting that probability  
14 of the aMTOC distribution increases from well center toward the edge. Middle histogram shows  
15 experimental probability of the aMTOC position in the absence of free tubulin and actin (n = 188  
16 wells). The probability tended to increase from well center toward the edge. However, the  
17 distribution near the edge was restricted, because of the size of aMTOCs (bead 1.5  $\mu\text{m}$  radius +  
18 MT seeds). Right histogram indicates probability per volume, suggesting almost random  
19 distribution of the aMTOCs in microwells. Volume per segment was calculated based on the  
20 approximate size of microwells (37.5  $\mu\text{m}$  in diameter and 20  $\mu\text{m}$  in height).

21 (B) Distribution of aMTOC in microwells at the indicated tubulin concentrations. Probability per  
22 volume was calculated as shown in (A). Data shown in Figure 1G were used.

23 (C) Time-lapse imaging of MT aster positioning at 18  $\mu\text{M}$  of tubulin shown in Figure 1H. In  
24 magnified images, the orange dots indicate the MTs hitting the well edge.

25 (D) Time-lapse imaging of MT aster positioning at 26  $\mu\text{M}$  of tubulin shown in Figure 1J. In  
26 magnified images, the blue and yellow arrow heads indicate the MTs slipping along the well edge,  
27 respectively.

28 Data information: Scale bar, 10  $\mu\text{m}$ .

29

30 **Figure EV3. aMTOC positioning in the presence of bulk actin network.**

31 (A) Distribution of aMTOC in microwells in the presence of the indicated tubulin and actin  
32 concentrations. Probability per volume was calculated as shown in Figure EV2A. Data shown in  
33 Figure 3B were used.

34 (B) The path-length (cumulative distance) of the aMTOC during the time-lapse imaging was  
35 measured for the indicated conditions. The data of individual aMTOC were shown with different  
36 colors (10 aMTOCs per condition). Images were taken at 1 min intervals.

1 (C) Distribution of the aMTOC in microwells in the presence of tubulin 26  $\mu\text{M}$  and bulk actin  
2 4  $\mu\text{M}$ . Probability per volume was calculated as shown in Figure EV2A. Data from Figure  
3 3B. Scale bar, 50  $\mu\text{m}$ .  
4 (D) Simulation in the presence of bulk actin network. Even with longer MT formation (compared  
5 to Figure 3E), the MTOC centering was not occurred. Different time points (75 and 250 sec) were  
6 shown. Right graph shows trajectories from blue (0 sec) to red (250 sec). MTOC, gray, MT, black,  
7 Actin, pink.  
8 (E) Simulations in the presence of lower density of actin. Different time points (25, 50, 100 and  
9 150 sec) were shown. Middle graph shows trajectories from blue (0 sec) to red (150 sec). Right  
10 graph shows final position of MTOC (at 150 sec). Data of the absence of actin (left) are same as  
11 shown in Figure 3G. ns (not significant) $>0.1$  (Mann-Whitney U test). 15 simulations per  
12 condition.  
13 (F) Simulations in the presence of smaller number of MTs. The images represent the time point  
14 at 150 sec. Right graph shows final position of MTOC (at 150 sec). \*\*\*\* $p<0.0001$  (Mann-  
15 Whitney U test). 15 simulations per condition.  
16 Data information: Violin plots were shown with the median (horizontal line).

17

18 **Figure EV4. Characterization of aMTOC positioning and MT behaviors in the absence or**  
19 **presence of cortical actin network.**

20 (A) Distribution of the aMTOC in microwells in the presence of the indicated tubulin and actin  
21 concentrations. Probability per volume was calculated as shown in Figure EV2A. Data shown in  
22 Figure 4B were used.  
23 (B) Time-lapse imaging of MT aster positioning at 26  $\mu\text{M}$  of tubulin in the presence of cortical  
24 actin shown in Figure 4F. Magnified images were shown. Scale bar, 10  $\mu\text{m}$ .  
25 (C) Orientation of MTs around the MTOCs in the absence or presence of cortical actin. The  
26 samples were same as shown in Figure 4E and F. Orientation of MTs were shown with different  
27 colors. Scale bar, 10  $\mu\text{m}$ .  
28 (D) Other representatives showing orientation of MTs near the well edge in the absence or  
29 presence of cortical actin. Orientation of MTs were shown with different colors. Right graph  
30 indicates the measurement of the MT orientation using Orientation J. The different time points  
31 were shown with different colors. Scale bar, 10  $\mu\text{m}$ .  
32 (E) The path-length (cumulative distance) of the aMTOC during the time-lapse imaging was  
33 measured for the indicated conditions. The data of individual aMTOC were shown with different  
34 colors (10 aMTOCs per condition). Images were taken at 10 min intervals.  
35 (F) Simulations of MTOC position over time in the absence (left) or presence (right) of cortical  
36 actin. 15 simulations per condition were shown with different colors.

1 **(G)** Simulations in the presence of smaller number of MTs. The images represent the time point  
2 at 200 sec. Right graph shows final position of MTOC (at 200 sec). \*\*\*\* $p < 0.0001$  (Mann-  
3 Whitney U test). 15 simulations per condition.  
4 **(H)** Distribution of the aMTOC in microwells in the presence of tubulin 18  $\mu\text{M}$  and cortical actin  
5 2  $\mu\text{M}$ . Probability per volume was calculated as shown in Figure EV2A. Data shown in Figure  
6 4B were used. Scale bar, 50  $\mu\text{m}$ .  
7 **(I)** aMTOC position in the presence of 26  $\mu\text{M}$  tubulin and with less dense cortical actin assembled  
8 at a lower concentration of actin (0.5  $\mu\text{M}$ ). Right panel shows measurement of distance from  
9 aMTOC to center of the well (2 hours after sample preparation).  $n = 71$  wells. Scale bar, 50  $\mu\text{m}$ .  
10 **(J)** Simulations in the presence of lower density of cortical actin. The time points at 200 sec were  
11 shown. Right graph shows final position of MTOC (at 200 sec). Data of the absence of actin (left)  
12 are same as shown in Figure 4M. ns (not significant) $>0.1$  (Mann-Whitney U test). 15 simulations  
13 per condition.  
14 Data information: Violin plots were shown with the median (horizontal line).

15

16 **Figure EV5. aMTOC positioning in the presence of asymmetric actin network.**

17 **(A)** Detection of actin inner zone. Actin 0.5  $\mu\text{M}$  and a-actinin 100 nM with Arp2/3 complex and  
18 NPF (WA) coating. The bottom and top were excluded from the maximum projection to visualize  
19 the vertical edges of actin. Using the partial max projection images and defining a threshold of  
20 actin intensity, the region of actin inner zone was detected and the center (centroid) was  
21 measured. Scale bar, 50  $\mu\text{m}$ .  
22 **(B)** Measurement of the fluorescence intensity of actin. The red arrow in the image indicates the  
23 region used for the line scan analysis. Right graph indicates the result of the line scan analysis.  
24 Background signals outside the wells were subtracted. The less actin region inside the cortex was  
25 defined as the actin inner zone. Scale bar, 10  $\mu\text{m}$ .  
26 **(C, D)** To analyze the aMTOC position with respect to the asymmetry of cortical actin, the angles  
27 from the well center to the center of the actin inner zone were aligned at the same degree ( $0^\circ$ ). It  
28 means that wells were reoriented in order to align the angles from the well center to the center of  
29 the actin inner zone.  
30 **(E)** Distance from aMTOC to well center (2 hours after sample preparation). Data shown  
31 in Figure 5E, F and I were used. (Tubulin 26  $\mu\text{M}$  Actin 0  $\mu\text{M}$   $n = 65$ , Tubulin 0  $\mu\text{M}$  Actin 0.5  $\mu\text{M}$   
32  $n = 74$ , Tubulin 26  $\mu\text{M}$  Actin 0.5  $\mu\text{M}$   $n = 79$  wells) \*\*\* $p < 0.001$ , \*\*\*\* $p < 0.0001$ , ns (not  
33 significant) $>0.1$  (Kruskal-Wallis test with Dunn's multiple comparison test). Violin plots were  
34 shown with the median (horizontal line).

1 **(F, G)** Distribution of the aMTOC in microwells in the presence of tubulin and actin at the  
2 indicated concentrations. Probability per volume was calculated as shown in Figure EV2A. Data  
3 shown in Figure EV5E and Figure 5J were used for (F) and (G), respectively.

4 **(H)** Simulations in the presence of asymmetric actin when the initial position was randomly  
5 chosen within 4  $\mu\text{m}$  from cell center. 25 simulations per condition. Different time points (From  
6 left, 25, 100 and 250 sec) were shown. Even if the initial position is off-centered, the MTOC  
7 tended to migrate toward the thinner side of the actin network. \*\*\* $p < 0.001$  (Mann-Whitney U  
8 test). Violin plots were shown with the median (vertical line).

9 **(I)** Simulations in the presence of smaller number of MTs. The images represent the time point at  
10 250 sec. Lower graph shows final position of MTOC (at 250 sec). 25 simulations per condition.  
11 Violin plots were shown with the median (vertical line).

12

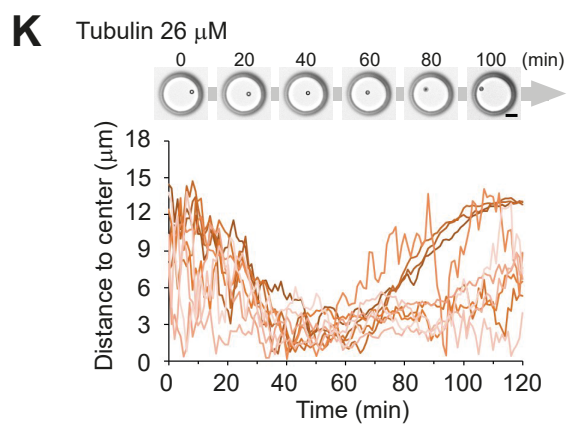
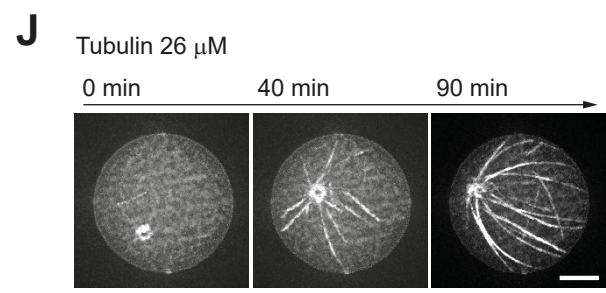
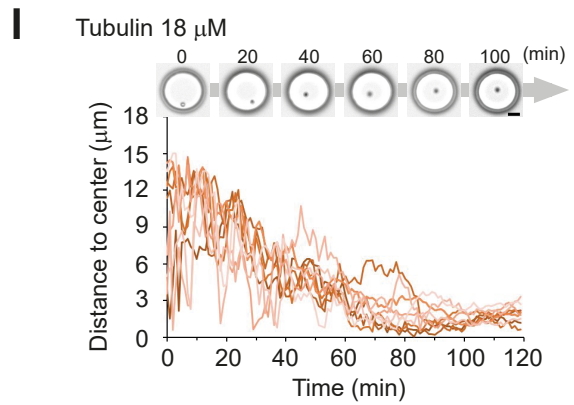
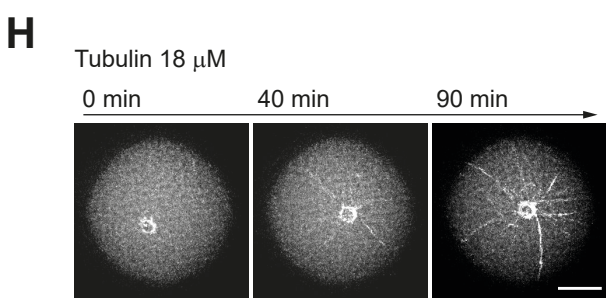
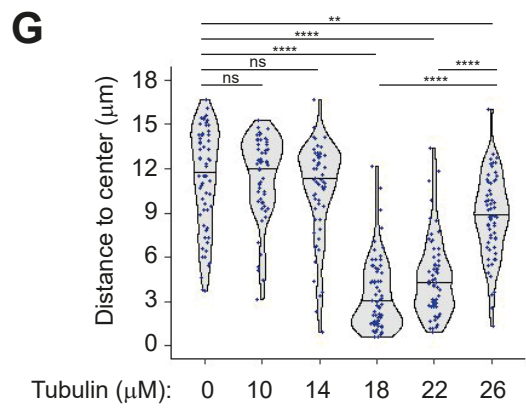
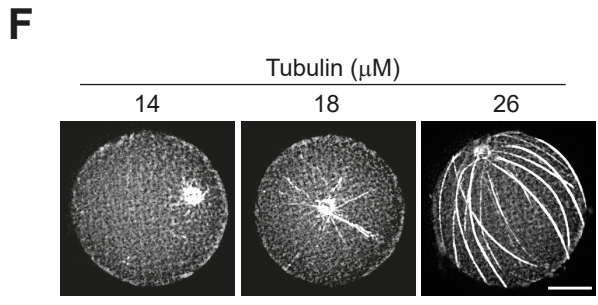
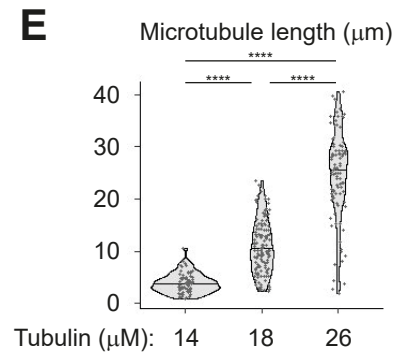
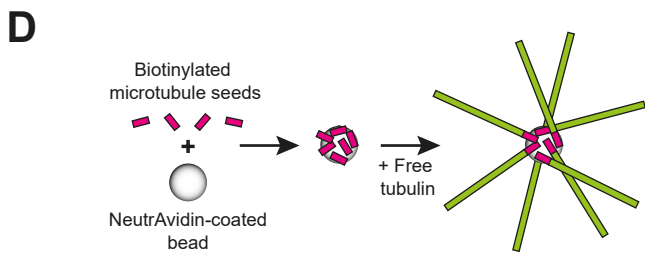
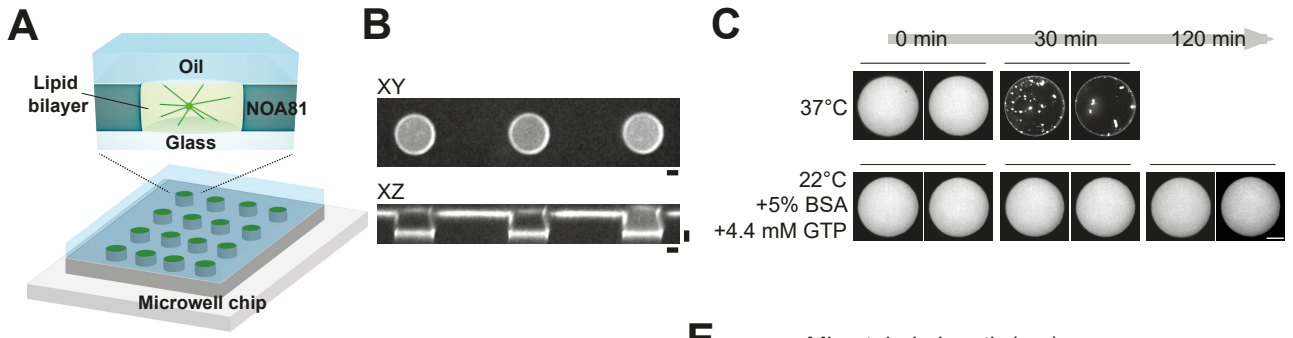
13

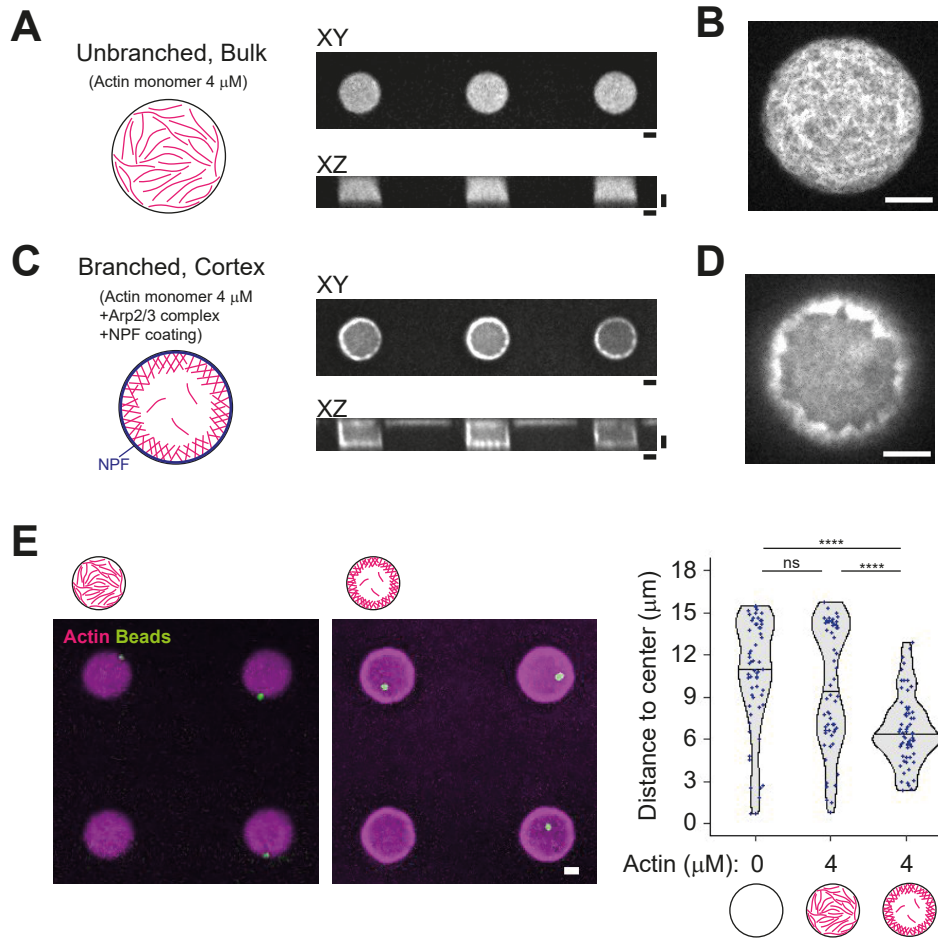
14

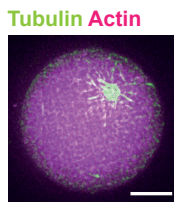
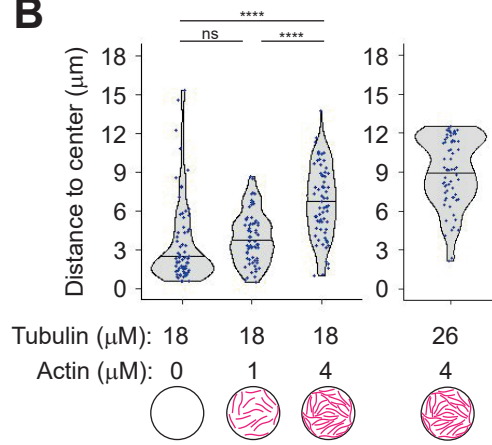
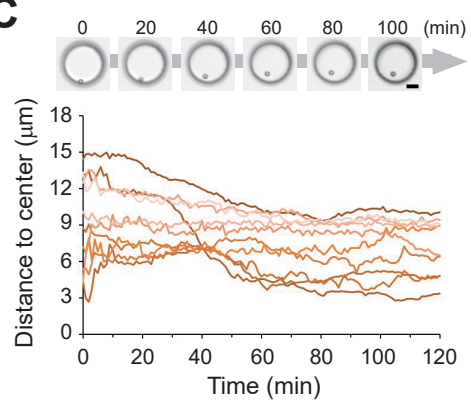
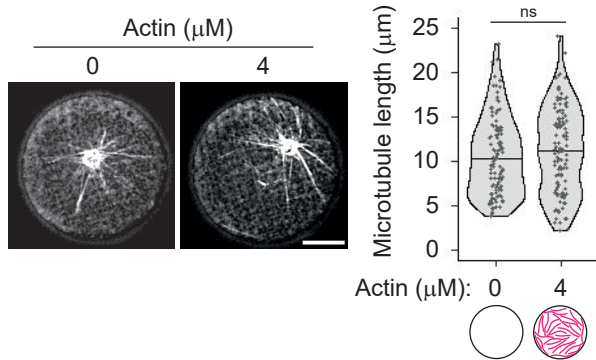
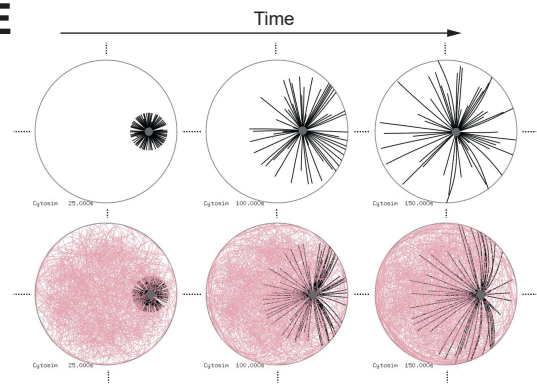
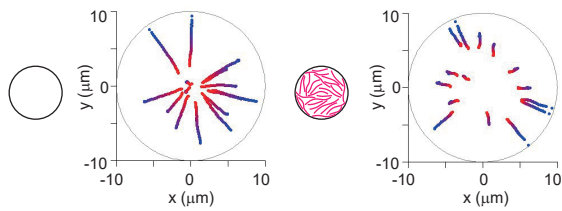
15

16







**A****B****C****D****E****F****G**